Hindawi
Advances in Civil Engineering
Volume 2023, Article ID 6634023, 16 pages
https://doi.org/10.1155/2023/6634023

Research Article

Finite Element Analysis of Corrosion Tubular T-Joint Repaired with Grouted Clamp

Peng Deng,[1,2] **Jian Guo**,[2] **Zhongyi Zhu**,[2,3] **Yan Liu**,[1,2] **and Qiang Zhu**[2]

[1]*Shandong Provincial Key Laboratory of Civil Engineering Disaster Prevention and Mitigation, Shandong University of Science and Technology, Qingdao 266590, China*
[2]*College of Civil Engineering and Architecture, Shandong University of Science and Technology, Qingdao 266590, China*
[3]*Beijing Institute of Architecture Design, Beijing 100055, China*

Correspondence should be addressed to Zhongyi Zhu; zhongyizhu05725@aliyun.com

Received 12 September 2023; Revised 6 November 2023; Accepted 27 November 2023; Published 29 December 2023

Academic Editor: Tafsir Tafsirojjaman

A finite element (FE) analysis of corroded circular hollow section T-joints repaired using grouted clamps is presented in this study. To ensure an accurate simulation, experiments on a T-joint with uniform corrosion and an intact T-joint with grouted clamp Deleted are reproduced separately using an FE model. The experimental and FE modeling results correlate closely, displaying similar failure behaviors and load–displacement responses. Subsequently, a total of 56 FE T-joint models with varying degrees of corrosion on the chord, repaired by grouted clamp, were then analyzed numerically. The corrosion was artificially applied to the chord's outer surface at depths of 10%, 20%, and 30% of the chord's thickness. The models also account for variations in joint geometry, dictated by parameters β and γ, which range from 0.565 to 0.678 and from 21 to 28, respectively. Furthermore, grouted clamp's properties were examined, including sleeve length, thickness, strength, as well as the thickness and strength of the grout, in relation to the complexity of the repair. The grouted clamp demonstrated significant repair capability, increasing the ultimate strength of the corroded joint by up to 2.23 times. Reinforcements that are both thicker and longer substantially enhance the joint's ultimate strength. However, inappropriate repair construction results in an abrupt termination of the load–displacement curve and a brittle failure phenomenon outside reinforced chord region. Additional weight from the grouted clamp requires reasonable control, and sleeve overlapping ratio should be guaranteed to be greater than 0.7. The joint bearing capacity can be efficiently increased by thicker grouts and sleeves only in ductile failure cases. The confinement effect and mechanism of the grouted clamp in joint deformation were visually analyzed as stress distribution from FE analysis results. Finally, a prediction equation is proposed to estimate the static strength of the repaired joint through regression analysis.

1. Introduction

Circular hollow section structures are prevalent in offshore engineering platforms owing to their favorable strength-to-weight ratio and low fluid drag coefficients [1]. However, these steel structures are highly susceptible to corrosion in marine environments, with offshore jackets experiencing general corrosion rates that lead to wall thickness loss ranging from 0.04 to 1.2 mm/year [2]. Anticorrosion coatings, guided by standards, such as DNV-OS-J101 [3] and ISO-19902 [4], are mandated to mitigate this issue. However, traditional protection methods [5] tend to fail after 15 years or less, leading to joint damage after extended periods of operation. To address this, reinforcement techniques have gained recognition as cost-effective methods for prolonging the lifespan of existing tubular structures, particularly given the high risks associated with the complete replacement of damaged members in marine settings. Conventional reinforcement methods for tubular joints typically involve welding metal stiffeners, such as collar plates [6–9], double plates [10, 11], or external rings [12]. Additionally, the use of fiber-reinforced polymer (FRP) has emerged as an excellent alternative for combating environmental corrosion and improving structural performance in terms of joint strength and stress distribution [13–19]. Current design guidelines, including GB-50017 [20], CIDECT [21], and EC3 [22], incorporate numerous provisions

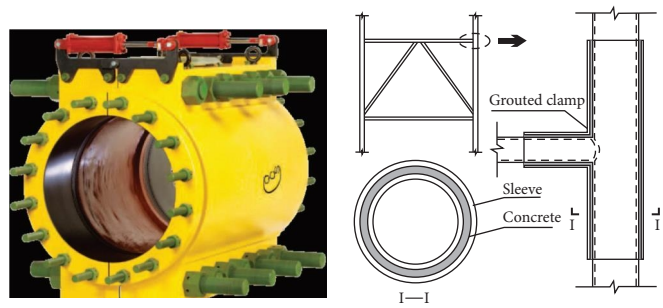

(a) (b)

Figure 1: Configuration of grouted clamp [31]. (a) Practical clamp component. (b) Sketch of grout clamp for T-joint.

for the reinforcement of joints, reflecting the advances and industry acceptance of these technologies.

Accident surveys [23] on offshore platforms revealed that corrosion can significantly degrade the stiffness and strength of structures, leading to structural failure at damage-prone locations. Wang and Shenoi [24] reported that pitting corrosion can lead to stress concentrations near affected areas. Additionally, Xu et al. [25] observed that corrosion at welds can cause a transition from ductile to brittle failure over time. The pattern of corrosion damage is often elusive, varying with both environmental conditions and time. Soares and Garbatov [26] established a correlation between the remaining strength of a structure and extent of corrosion loss, although the findings were specific to certain types of corrosion. To contend with the complexities of corrosion damage, the American Society of Mechanical Engineers has issued a manual [27] addressing corroded pipelines, which presupposes that long-term corrosion manifests as having an average maximum depth. Building on these widely accepted principles, researchers [28–30] have simulated uniform corrosion on tubular structures to study the mechanical impacts on damaged joints.

To address the issue of reinforcing joints that have been compromised by damage, grouted clamps have been considered as a viable solution. As illustrated in Figure 1, this type of stiffener is constructed from two or more half-precast clamp sleeves, customized to the joint's configuration, followed by the injection of grout into the space that is reserved for this purpose. Since its initial use in the mid-1970s, the technology of external grout reinforcement has become prevalent in offshore structures. Notably, in Europe, offshore wind platforms that utilize sleeve-grouted technology with large diameters represent 60% of the industry [31]. A grouted clamp that has been reinforced can bridge loads over the compromised area, mitigate fatigue sensitivity, and offer a relatively straightforward installation process. The stiffness of the confined grout surpasses that of conventional grout [32], and the structural capacity to withstand cracks in T-joints is heightened in correlation with the grout's compressive strength [33]. In comparison to other reinforcement methods using metal or FRP, grout serves as an ideal addition to counteract wall thickness lost to corrosion, averts potential damage from welding, and maintains the desirable strength-to-weight ratio of tubular structures through partial reinforcement. Jiang et al. [34] noted that adjusting the size of the sleeve can alter the joint's failure mode and increase resistance to deformation. However, Chilvers [35] observed that lengthening the sleeve might not significantly enhance the contribution of the grout. CIDECT [21] offered a standard strength equation for the long-term examination and usage of grout-filled joints. However, the theoretical model provided by CIDECT [21] does not account for the effects of corrosion, which could substantially compromise joint integrity.

In this study, the static behavior of uniformly corroded tubular joints repaired using grouted clamps is comprehensively investigated both numerically and analytically. Experimental tests were performed using a finite element (FE) model to validate the applicability of the simulation, and 56 numerical models of corroded joints with grouted clamps were employed. A parametric analysis was performed to investigate the effects of the joint geometry, corrosion degree, and grout clamp parameters on the ultimate strength and failure modes.

2. Modeling and Verification Method

2.1. FE Verification Strategy and Model Producing. Owing to a scarcity of experiments on corrosion-affected T-joints repaired with grouted clamps, FE verification was conducted based on relevant experimental studies. Specifically, a uniformly corroded joint (T-1) fabricated as reported by Shao et al. [29], along with a reinforced intact joint equipped with a grouted clamp (ZHU2) as produced by Jiang et al. [34], was selected for the verification process discussed in this paper. The rationale behind the selection of these experimental specimens was twofold: both specimens underwent identical testing procedures to assess the compressive performance of the T-joint, and they shared similar material properties.

Specimens were replicated to validate their load–displacement trajectories and failure modes, thereby confirming the effectiveness of the FE simulation. Subsequently, FE models for corroded T-joints repaired with grouted clamps were developed. The commercial software package Abaqus [36] was utilized for all modeling activities.

Table 1 presents the measured geometric dimensions for specimens T-1 and ZHU2. Owing to T-1's perfect symmetry, a half-model with symmetric boundary conditions was adopted to decrease computational demand of time. The geometry of the

Table 1: Geometry properties of T-1 [29] and ZHU2 [34] (unit: mm).

Specimen	Brace			Chord			Corrosion		Grouted clamp		
	b_1	t_1	L_1	b_0	t_0	L_0	Length	Depth	t_c	t_s	α
T-1	95	4	536	168	5	1,960	520	1.5	–	–	–
ZHU2	114	6	750	168	8	1,500	–	–	7	6	1

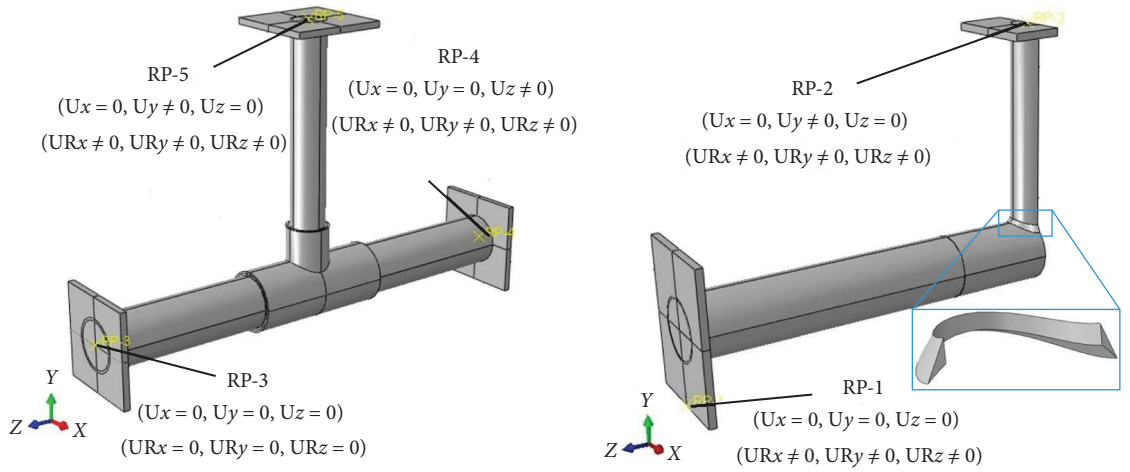

Figure 2: Geometrical properties and boundary conditions of verification models used in the present study: (a) T-1 and (b) ZHU2.

Table 2: Material properties of T-1 [29] and ZHU2 [34].

Specimen	Part	E (MPa)	f_y (MPa)	f_u (MPa)
T-1	Chord	200,000	386.00	–
	Brace	200,000	345.00	–
ZHU2	Chord	220,543	302.18	457.48
	Brace	207,869	348.43	565.87

weld was acknowledged to significantly influence the yield line [37] and resistance capacity of the joint [37]. A weld model conformed to the GB-50017 standard [20] was incorporated into all models within this study.

For ease of application, the reference point (RP) control method [38] was employed, with the specific boundary conditions depicted in Figure 2. The cut surface of T-1 was arranged on a symmetric boundary rather than at an RP. The interaction between the grouted clamp and joint surface was modeled using the Coulomb friction model [39], assuming a friction coefficient of 0.6 for tangential behavior and characterizing the normal contact as hard.

2.2. Material Properties of the Verification Model. The material properties of the steel components are summarized in Table 2. The von Mises plastic criterion and bilinear isotropic strain-hardening plasticity model [36] were adopted for the steel chords, braces, and clamps. The nonlinear concrete damage plasticity (CDP) constitutive model [36] combined with plasticity theory and damage mechanics allows the prediction of inelastic concrete behavior via simulation. Specifically, the CDP model is ideal for damage analysis based on scalar damage elasticity. Furthermore, it allows for a precise definition of the fracture performance of the grout [40, 41]. The dilation angle for the major plasticity parameter was set to 30°, whereas default values were used for other parameters [36].

2.3. Elements and Mesh of the Verification Model. Shell elements have been widely used in tubular joint analysis [37] to achieve efficient computations. Previously, the application of a solid element was advocated to reflect the realistic weld interface. An eight-node brick element with reduced integration (C3D8R) [36] was selected to build all members.

The meshing strategy strikes a balance between computational efficiency and the need for convergence in the study. To ensure the accuracy of the simulations, the mesh was partitioned into subzones, each with a tailored mesh size. The employed meshing approach is detailed in Figure 3. In the area where the members intersect, a mesh with dimensions of 5 mm × 5 mm (length × width) was utilized. For the transitional area between the corroded and intact sections of the chord, a finer mesh of 5 × 1 mm was applied. Other areas, not specifically mentioned, were assigned a coarser mesh size to expedite computational processes. The chord's wall thickness direction necessitated a three-layer mesh to stabilize the through-thickness stress, as indicated by previous findings [42]. The mesh across the model was generated with a predominance of hexahedral elements, employing a structured meshing technique for global mesh development.

2.4. Modeling Result and Verified Process. According to Lu et al. [43], the joint ultimate strength is related to the

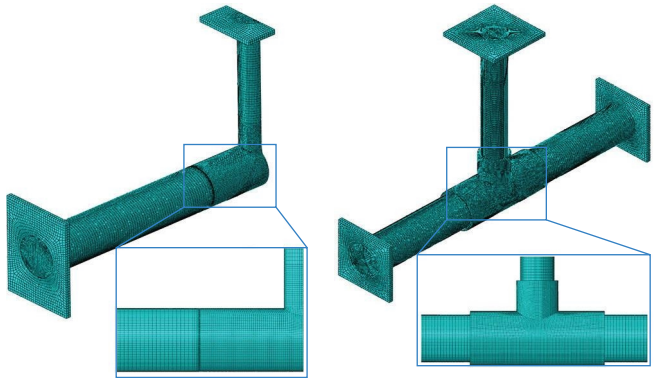

(a) (b)

Figure 3: Mesh arrangement of verified models: (a) T-1 and (b) ZHU2.

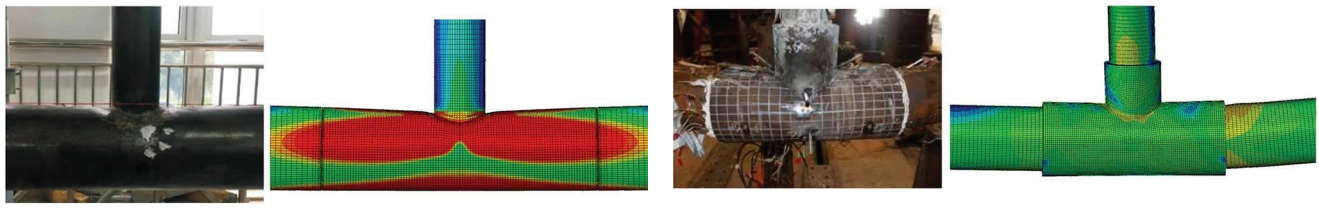

(a) (b)

Figure 4: Comparison of failure modes between models and experiments. (a) Failure status verification of T-1. (b) Failure status verification of ZHU2.

load–displacement curve. The most significant peak load is regarded as the value of the ultimate strength; however, if it is not reflected in the load–displacement curve, then the load value corresponding to a displacement of 3% of the chord thickness is used as the deformation serviceability limit. Specifically, the repaired chord thickness is ambiguous because it can be altered by corrosion or reinforcement. The original chord wall thickness d_0 is typically applied and adopted for this type of investigation.

The contrasting failure modes of the model and specimen are shown in Figure 4. The simulation results show a postfailure appearance analogous to that of the experiment. T-1 and ZHU2 exhibited a typical failure process under compression. For T-1, the compressive force from the brace led to increased concavity in the chord, culminating in the formation of a plastic hinge line around the intersection area (Figure 4(a)), in alignment with the zones of high-stress concentration. In the ZHU2 model, minimal bending of the chord was observed under brace compression until it approached 95% of the maximum load, beyond which noticeable deformation appeared at the sleeve's end. The final deformation of the ZHU2 model at the peak of the load–displacement curve closely resembled that of the corresponding experimental specimen. The load–displacement curves are presented in Figure 5, with "EX" denoting experimental data and "FE" indicating simulation data. During the elastic phase, the load–displacement responses of T-1 and ZHU2 models mirrored those of the corresponding specimens. Although the models showed slightly less deflection in the plastic phase when compared to the experiments, the discrepancies were within an acceptable range. The ultimate strength of the T-1 model attained 98.30% of the experimental specimen's value (Figure 5(a)), and the ZHU2 model reached 94.19% of its experimental counterpart's strength (Figure 5(b)). Accounting for potential sources of error, the models corresponded closely with the experimental data, rendering the results credible. Consequently, the validation confirms the capability of the FE models to accurately simulate the mechanical behavior of corroded T-joints reinforced with grouted clamps.

3. Numerical Modeling Program

3.1. Scope. In this study, three types of joint models were created (i.e., original (U), corroded (D), and corrosion-reinforced (DR) joint). Four original T-joints (U) with different geometric properties were designed. The geometries of the corroded and repaired joints differed from those of the original joints. The models of the repaired joint were cut into circumferential grooves [27] on the chord surface (Figure 6(a)) and a grouted clamp [44] was fabricated (Figure 6(b)) to fill the corroded thickness. The corrosion length of all models was 600 mm along the chord axial direction, and the uniform depth of the groove became a variable reflecting the corrosion degree of the repaired joints. Corrosion joints (D) were carved in a groove with 10% chord thickness (Per = 0.1). Various parameters associated with the geometry and material properties were investigated (i.e., the original T-joint geometry, corrosion degree, grouted clamp geometry, and grouted clamp material).

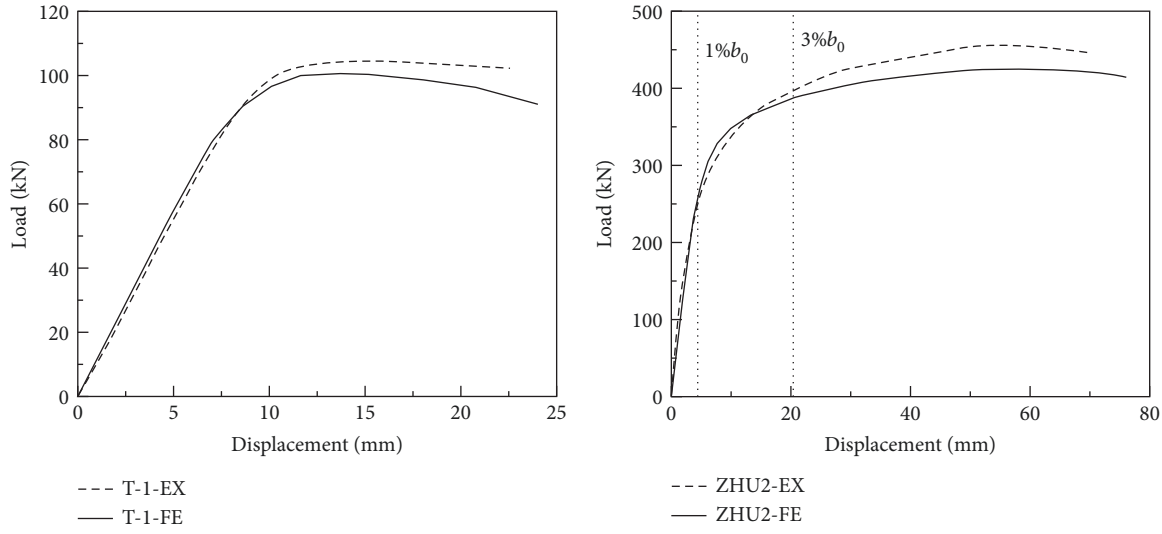

Figure 5: Comparison of load–displacement curves between models and experiments: (a) T-1 and (b) ZHU2.

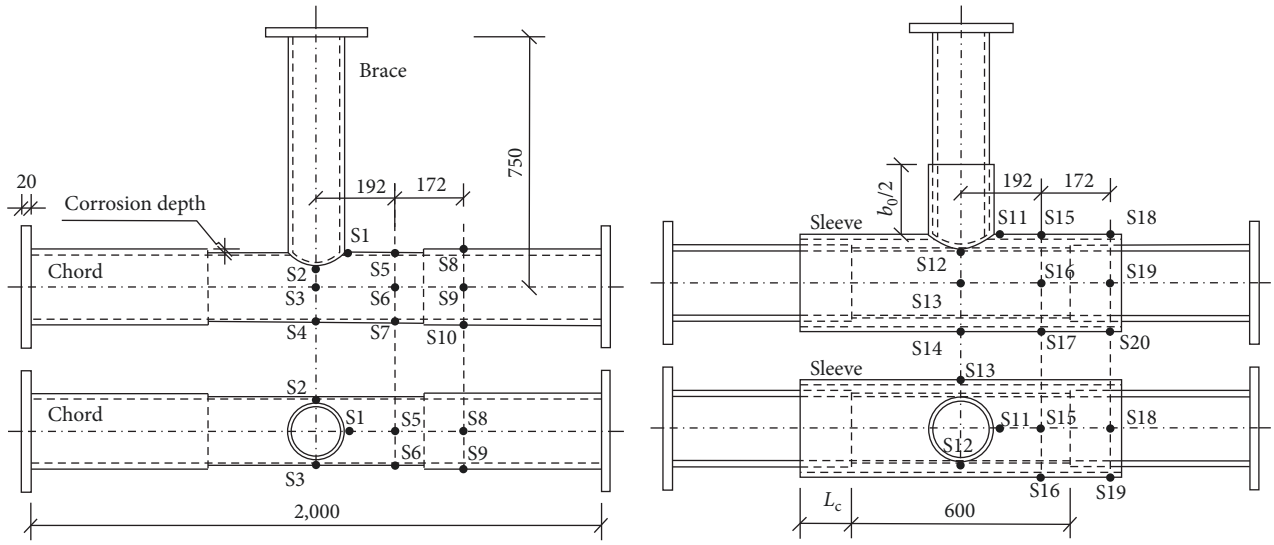

Figure 6: Dimensions and monitor arrangement of the numerical model (units: mm): (a) corroded joint and (b) repaired joint.

To ensure a credible simulation results, the investigated scope of joint sizes was based on ZHU2 [34], which was scaled down from a practical offshore platform. The governing geometrical parameters of β and γ were conservatively extended (i.e., β and γ were varied from 0.565 to 0.678 and 21 to 28, respectively). The chord and brace lengths of all the models were set as fixed values, as shown in Figure 6. Furthermore, d_0 and t_1 values of all models were set to 168 and 6 mm, respectively. Moreover, T_1 and T_2 indicated the same t_0 value of 6 mm, whereas T_3 and T_4 indicated a t_0 of 8 mm. Additionally, T_1 and T_3 indicated the same b_1 value of 95 mm, whereas the other joints indicated a b_1 value of 117 mm.

The material characteristics for the chord and brace replicated those utilized in the ZHU2 model [34]. The reinforcement effectiveness of a tubular joint is substantially reliant on the material strength of the grouted clamp [45]. Consequently, various commonly employed material categories were examined. Multiple grades of grout [46]—specifically C15, C20, and C30—alongside steel sleeves conforming to the standards of Q235 and Q345 [20] were employed in the analysis. The material specifications for the grout were derived from the concrete damaged plasticity (CDP) model and related research by Costa and Gidro [47]. The data for the clamp materials encompassed Young's modulus, yield strength, and tensile strength; for clamp Q235 [48] and Q345 [49], these parameters were 210, 334, and 480 MPa and 210, 499, and 596 MPa, respectively.

3.2. Numerical Model Information. Fifty-six FE models were developed, with their design parameters listed in Table 3. The analysis delved into six variations of the DR joint, which

Table 3: Geometry property arrangement of numerical models.

Model	Corrosion degree	Grout construction		Sleeve construction		
		C	t_c (mm)	Q	t_s (mm)	α
$T_1/T_2/T_3/T_4$-U	–	–	–	–	–	–
$T_1/T_2/T_3/T_4$-D	0.1	–	–	–	–	–
$T_1/T_2/T_3/T_4$-DR-*P*	0.1/0.2/0.3	C30	7	Q345	6	0.5
$T_1/T_2/T_3/T_4$-DR-L	0.1	C30	7	Q345	6	0.5/0.7/1
$T_1/T_2/T_3/T_4$-DR-C	0.1	C15/C20/C30	7	Q345	6	0.5
$T_1/T_2/T_3/T_4$-DR-CT	0.1	C30	7/14	Q345	6	0.5
$T_1/T_2/T_3/T_4$-DR-LCT	0.1	C30	7/14	Q345	6	1
$T_1/T_2/T_3/T_4$-DR-Q	0.1	C30	7	Q235/Q345	6	0.5
$T_1/T_2/T_3/T_4$-DR-ST	0.1	C30	7	Q345	6/8	0.5
$T_1/T_2/T_3/T_4$-DR-LST	0.1	C30	7	Q345	6/8	1

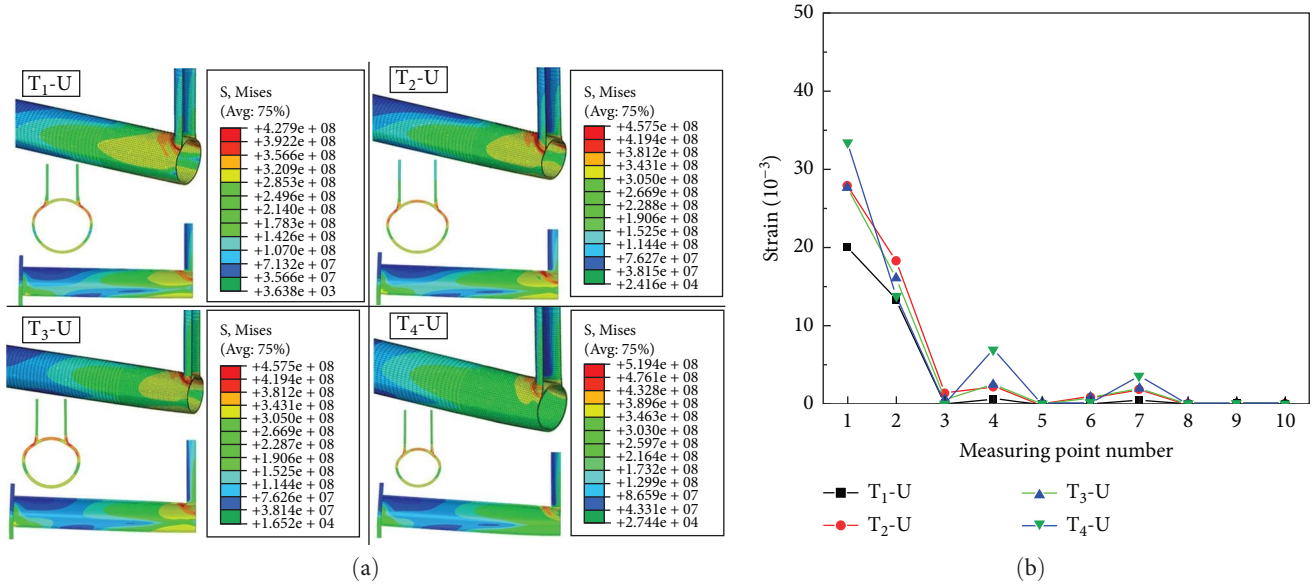

Figure 7: Stress contours and equivalent plastic strain of original joints. (a) Stress contours of original joints. (b) Equivalent plastic strain of original joints.

were distinguished based on aspects of the grouted clamp complexity. These aspects included the compressive strength of the grout (C), thickness of the grout (t_c), thickness of the sleeve (t_s), tensile strength of the sleeve (Q), and sleeve length coefficient (α). Additionally, three different levels of chord thickness corrosion percentage ($P = 0.1$, 0.2, and 0.3) were examined. The models of the repaired joints were categorized into eight series (DR-P, DR-C, DR-CT, DR-ST, DR-Q, DR-L, DR-LCT, and DR-LST), where LCT and LST signify the variations in the thickness of the grout and sleeve for the elongated sleeve ($\alpha = 1$). In the nomenclature for the repaired model variants, the suffixes denote the specific characteristics of the grouted clamp. For instance, the term T_1-DR-$P_{0.1}$ denotes a model where the corrosion depth is $10\%d_0$.

3.3. Strain Measurements. Twenty monitors, labeled S1–S20, were distributed (Figure 6) to analyze the equivalent plastic strain. In particular, S1–S10 were assigned to the surface of the chord, and S11–S20 were used to measure the strain development on the clamp surface. The monitors were positioned on only one-quarter of the model owing to the model symmetry. The distribution near the weld was 20 mm from the edge of the weld model. The chord indentation value on the load–displacement curve was obtained by subtracting the chord bend deflection from the downward displacement of the brace [50].

4. Results

4.1. Original and Corroded Joints. As the axial load increased, chord indentation occurred and the sidewall gradually bulged outward. The ultimate strengths [43] of the original and corroded joints were determined when the chord indentation reached $3\%d_0$. The stress concentration (Figure 7(a)) was high near the intersection line and gradually dissipated within the effective chord length [51]. The maximum value of the equivalent plastic strain (Figure 7(b)) was observed at the crown (S1) and saddle (S2) points; however, the strain

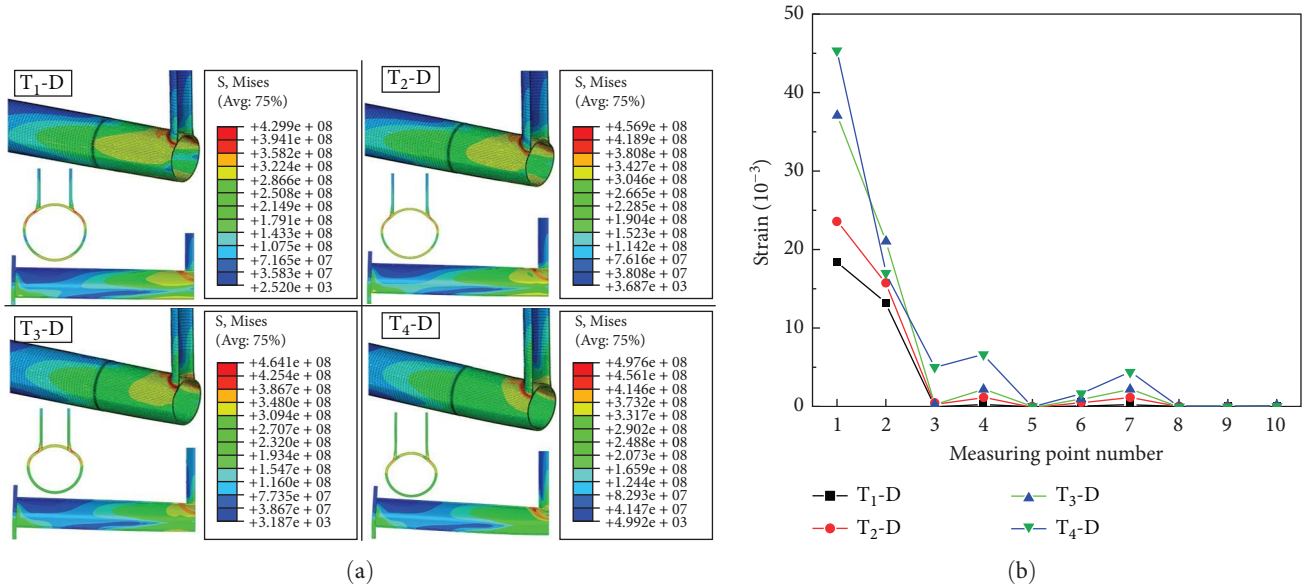

FIGURE 8: Stress contours and equivalent plastic strain of corroded joints. (a) Stress contours of corroded joints. (b) Equivalent plastic strain of corroded joints.

values at the other locations did not exceed the chord yield strain. The progressive plastic evolution revealed local characteristics in the vicinity of the intersection area, which is consistent with the observations of Zhao et al.'s [52] study.

The joint appearance and stress contours (Figure 8(a)) of the corroded joints were similar to those of the dependent intact joints at the ultimate strength. However, the chord indentation in the intersection region of the corroded joints was magnified when the chord thickness was reduced. Additionally, the thickness reduction resulted in a lower equivalent plastic strain (Figure 8(b)) at the crown point (S1) than at the dependent intact joint. For T_1-U, the strain value of S1 was 31.5% higher than that of T_1-D. However, other monitors did not show results that were significantly different from those of T_1-D. The failure modes of the original and corroded joints were controlled by the local indentation of the chord in the intersecting area (LIC) [21]. This is consistent with the findings of Benjamin and Andrade [27], who noted that a slightly reduced t_0 does not significantly affect the failure mode.

4.2. Reinforced Joint. Based on the simulation results for all repaired joints, three distinct typical failure phenomena occurred on the joint surface: LIC, plastic hinge at the sleeve end (PHSE), and elliptical deformation of the chord in the intersecting area (EDC). Extensive ductile compression (EDC) and LIC were both induced by chord indentation but at different deformation levels in the ring section. Furthermore, EDC typically appears in compound mode with PHSE (EDC + PHSE). In addition to the failure of the joint surface, the grout section exhibited clear destruction. Grout failure may encompass compressive destruction around the sleeve end, compressive destruction around the intersection region, and separation between the grout and joint surface. The failure of the joint and grout exerts a significant effect because of the synergy between the joint and grouted clamp. The failure of the joint surface with the PHSE was followed by the aforementioned three grout destruction modes. The LIC and EDC underwent grout destruction only near the intersection region. Therefore, the failure modes of the repaired joint were dominated by joint surface failure (LIC, PHSE, EDC, and EDC + PHSE).

After a meticulous examination, three representative models, T_1-DR-$P_{0.1}$, T_4-DR-$P_{0.1}$, and T_1-DR-L_1, which correspond to the joint failure modes of PHSE, EDC + PHSE, and LIC, respectively, were selected for investigation. A chord indentation value corresponding to $3\%d_0$ was adopted as the ultimate strength of the repaired joints [43]. The stress contours and equivalent plastic strains were extracted based on the ultimate strengths of representative models. The compressive damage (damage) of the grout in three progressive stages (grout destruction at the first moment, midtransition stage, and the stage corresponding to the ultimate strength of the joint) was investigated.

4.3. T_1-DR-$P_{0.1}$. In the elastic stage of the load–displacement curve (Figure 9(a)), the joint with the grout clamp exhibited higher stiffness than the unrepaired joint. The peak load of T_1-DR-$P_{0.1}$ was greater than that of the corroded specimen; however, the chord indentation did not reach $3\%d_0$ during the loading process. For the joint failure mode of the PHSE, a specific rotation abruptly substituted the chord indentation, which caused an abrupt decrease in the load–displacement curve after the peak point. Given that the subsequent load response of the joint is transferred to the sleeve end, the chord indentation value remains constant, and the further development of the curve, as shown in Figure 9(a), is terminated. The equivalent plastic strain (Figure 9(b)) on the chord surface primarily developed at the saddle point (S2) and end of the sleeve (S8, S10). The strain development in the intersection region was less significant than that in the unrepaired region. The maximum value of S10 corresponds

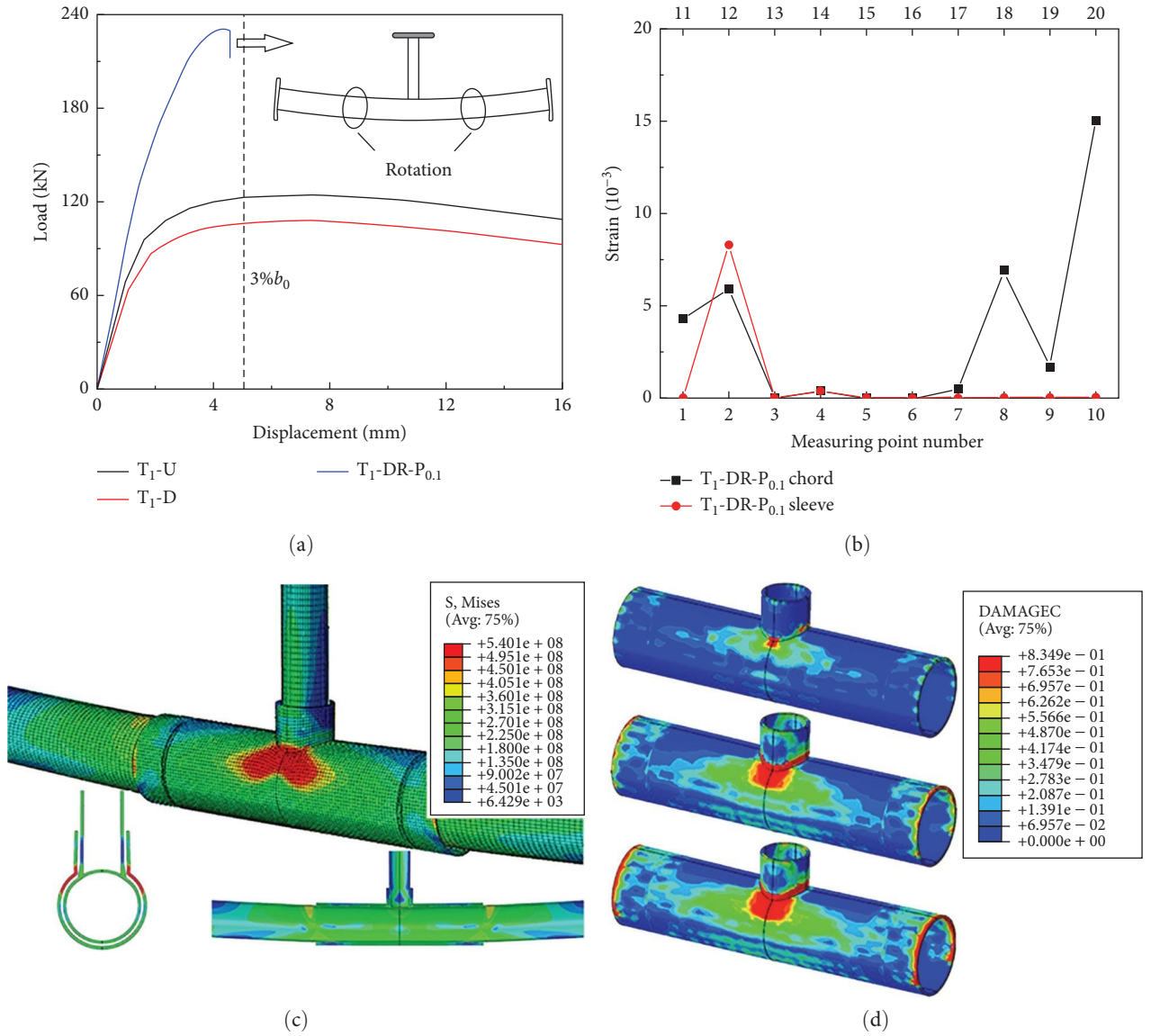

FIGURE 9: Load–displacement curve, equivalent plastic strain, stress contours, and grout damage of T_1-DR-$P_{0.1}$. (a) Load–displacement curves comparison to T1-U, T1-D. (b) Equivalent plastic strain on ultimate strength status. (c) Stress contours on ultimate strength status. (d) Grout damage evolution.

to the rotation at the sleeve end. The major effect of the grout clamp was the lateral restraint on the joint sidewall bulge [34]. The strain distribution on the clamp surface exhibited a primarily stable increasing trend with a marked peak at the saddle point (S12).

Plastic deformation is predominantly concentrated in the chord adjacent to the sleeve end, as depicted in Figure 9(c). Owing to the composite bending and rotation occurring at the sleeve end, detachment of the chord from the lower grout layer was observed. Once this rotation was initiated, the confined joint, reinforced by the grouted clamp and functioning as a rigid body, displayed increased brittleness. Consequently, the resultant chord indentation exceeded the allowable service limit of $3\%d_0$, and no discernible ovalization was apparent in the ring section. The progression of grout damage, as shown in Figure 9(d), originates from the intersection region, extending mainly along the chord sidewall, with the upper grout near the sleeve end experiencing significant deterioration. Although the application of the grouted clamp resulted in a heightened peak load, the grout demonstrated a sudden brittle failure. Hence, the observed PHSE failure mode is considered to be impractical for engineering applications.

4.4. T_4-DR-$P_{0.1}$. A plastic hinge and rotation were observed in the vicinity of the sleeve end; meanwhile, the joint deformation of T_4-DR-$P_{0.1}$ was affected more clearly around the intersection region. The enlarged β of T_4-DR-$P_{0.1}$, when compared with that of T_1-DR-$P_{0.1}$, resulted in a lower chord stiffness [37]. The load–displacement curves in the elastic stage (Figure 10(a)) were similar to that of T_1-DR-$P_{0.1}$. Although the load–displacement curves indicated sudden joint failure, the

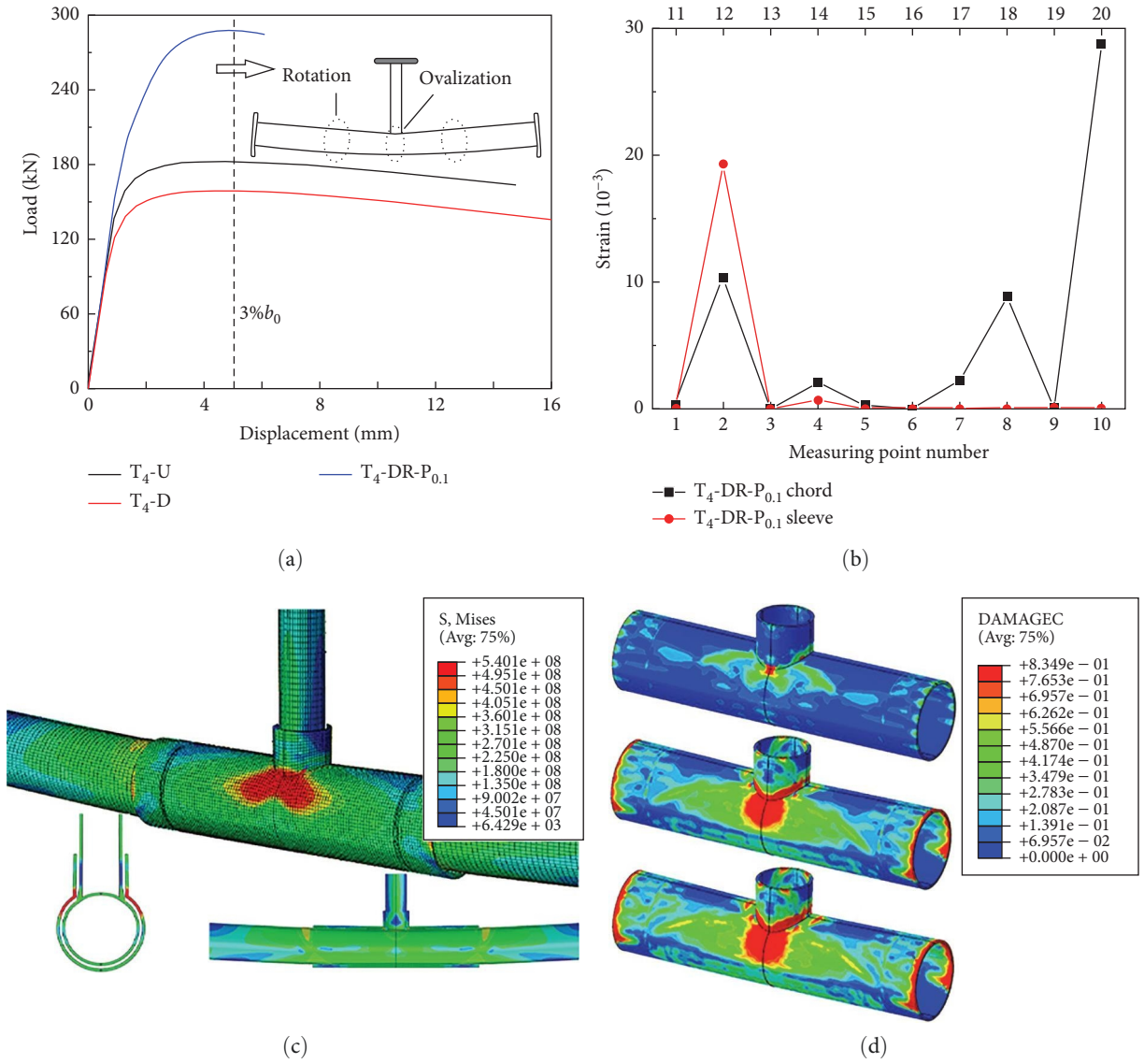

FIGURE 10: Load–displacement curves, equivalent plastic strains, stress contours, and grout damage of T_4-DR-$P_{0.1}$. (a) Load–displacement curves comparison to T4-U, T4-D. (b) Equivalent plastic strain on ultimate strength status. (c) Stress contours on ultimate strength status. (d) Grout damage evolution.

chord resisted a greater load than T1-DR-P0.1, with deformation surpassing the 3%b_0 benchmark. As illustrated in Figure 10(b), the global strain of T4-DR-P0.1 was significantly more pronounced than that of T_1-DR-$P_{0.1}$. The maximum equivalent plastic strain was observed at S10 owing to considerable rotation near the sleeve end. In the intersection region, the strain at saddle points (S2, S12) for T_4-DR-$P_{0.1}$ was nearly double that observed for T_1-DR-$P_{0.1}$, while the strain at the crown point (S1) of T_4-DR-$P_{0.1}$ was virtually nil. When compared to T_1-DR-$P_{0.1}$, the strain development of T_4-DR-$P_{0.1}$ showed marked improvement in areas, such as S4 and S7, within the confined space. Despite the significant rotation at the sleeve end causing noticeable strain at S19 and S20, the strain in the middle of the chord sidewall remained zero.

The geometric alteration of T_4-DR-$P_{0.1}$ resulted in more evident ovalization than that exhibited by T_1-DR-$P_{0.1}$ in the ring section, as shown in Figure 10(c). Given the joint lateral expansion in the vicinity of the intersection region, the grouted clamp tended to swell outward. In terms of the brace root, a slight separation between the joint and grout appeared in this severe joint bulge. Furthermore, the grout exhibited a high degree of damage, as shown in Figure 10(d). However, in the vicinity of the sleeve end, the bottom area of the grout did not contribute to the load resistance because the separation from the joint was similar to that exhibited by T_1-DR-$P_{0.1}$.

The plastic behavior of T_4-DR-$P_{0.1}$ under (EDC + PHSE) improved significantly when compared with that under PHSE, and the grout contributed more to the load resistance. However, the PHSE resulted in brittle failure.

4.5. T_1-DR-L_1. The failure mode of the LIC on the repaired joint exhibited ductile and predictable plastic features [53]. A gentle plastic stage emerged in the load–displacement curve (Figure 11(a)), and the curve characteristics of T_1-DR-L_1

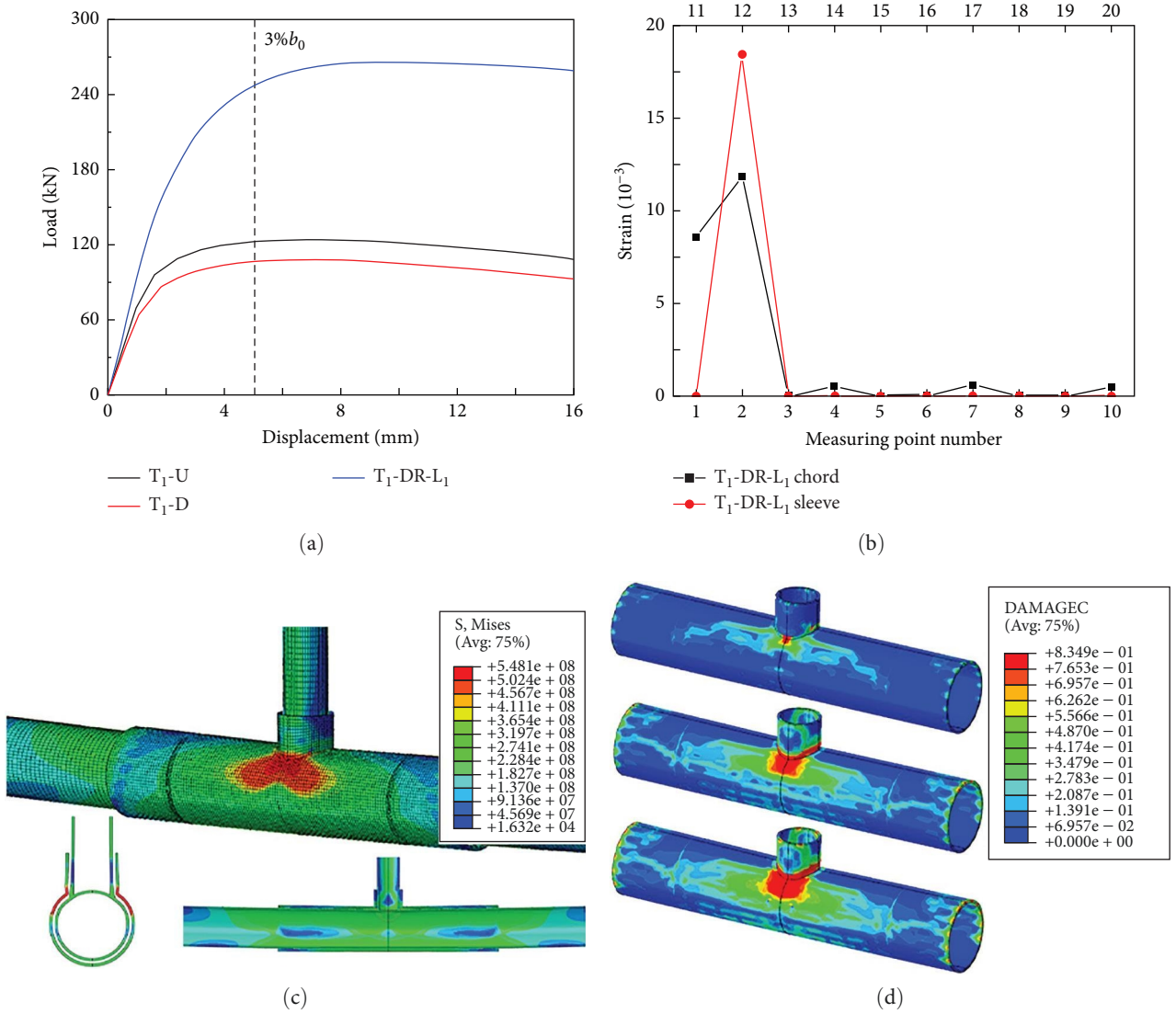

FIGURE 11: Load–displacement curves, equivalent plastic strains, stress contours, and grout damage of T_1-DR-L_1. (a) Load–displacement curves comparison to T1-U, T1-D. (b) Equivalent plastic strain on ultimate strength status. (c) Stress contours on ultimate strength status. (d) Grout damage evolution.

were similar to those of T_1-U. The repair efficiency of T_1-DR-L_1 was the highest among the three representative models, in which the ultimate strength of T_1-DR-L_1 increased by 129.2% when compared with that of T_1-D. In terms of the equivalent plastic strain (Figure 11(b)), only the saddle (S2 and S12) and crown (S11) regions exhibited significant development. Apart from the intersection region, other locations including the sleeve end area exhibited extremely low strain values.

Owing to the absence of rotation at the sleeve end, joint deformation occurred at the intersection region. Clear global bend and chord indentation are observed, as shown in Figure 11(c). Stress concentration (Figure 11(c)) and grout damage occurred primarily in the area around the intersection region. Owing to the concentrated load response and longer reinforcement length of T_1-DR-L_1, a smaller damage range is observed, as shown in Figure 11(d).

The threatened yield hinge for joint failure under the LIC was dispersed, and the destruction phenomenon revealed localized ductility. The failure mode of the EDC exhibited ductile behavior in the intersection region; however, the deformed ring section approached ovalization much earlier than the LIC. In general, the LIC and EDC are attractive failure modes for repaired joints, and their mechanisms are discussed in the following section.

4.6. Analysis of Failure Mode. The simulation results for the original and corroded joints supported the failure criterion of chord plastification proposed by CIDECT [21] and EC3 [22]. However, a joint with a grouted clamp allows another destruction path [34]. If a plastic hinge emerges on the chord at the sleeve end, then joint failure is determined by the partial chord material strength [54] instead of the reinforced section. In engineering applications, failure involving a PHSE should be

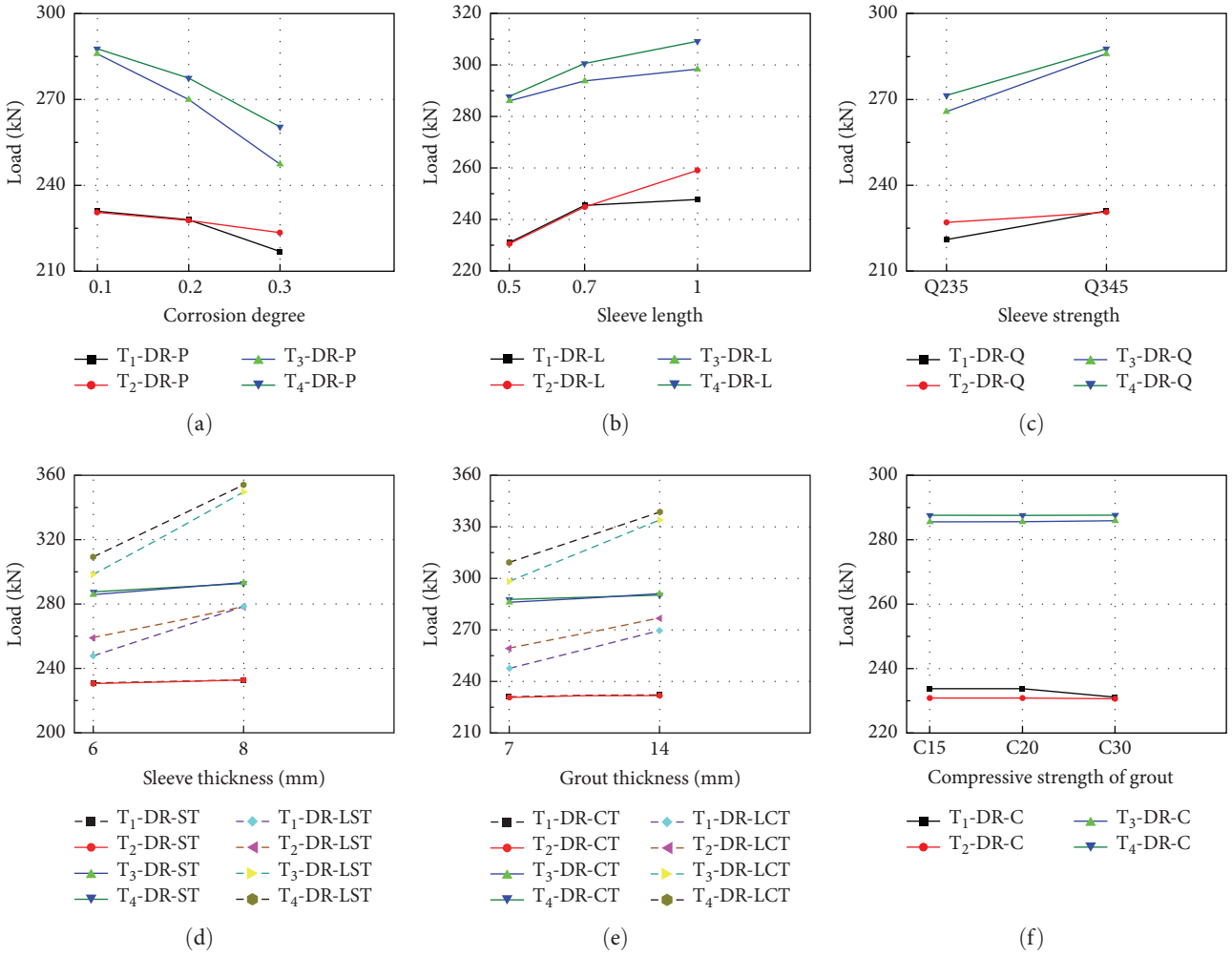

FIGURE 12: Joint strength effects of corrosion and grouted clamp parameters. (a) Strength effect of Per. (b) Strength effect of α. (c) Strength effect of Q. (d) Strength effect of t_s. (e) Strength effect of t_c. (f) Strength effect of C.

avoided in repaired joints, i.e., only LIC and EDC are acceptable failure modes.

The destruction of the grout was initiated at the intersection of the joint subjected to loading from joint deformation. The damage aggravation of the grout in all failure modes continued to the sidewall via the chord bulge and expanded marginally along the direction of the chord axis. Regarding the PHSE, the bottom grout separated from the joint and did not participate in the process.

The compressive load on the brace resulted in a global bend in the chord [55], and a joint with additional weight from the grouted clamp intensified the deflection. The bending of the reinforced chord region was primarily limited [44] because of the deformation restraint of the gout clamp. However, the use of a bare chord to ensure the locality of the reinforcement resulted in an uncoordinated deflection trend [44]. Hence, rotation and plastic hinges appeared on the chord at the sleeve end, causing the accumulation of brittle failure. As part of the deflection incompatibility region, the end sleeve of the chord should exhibit a relatively small bending magnitude. The grouted clamp weight was maintained within a controlled range. In terms of the complexity parameters of the grouted clamp, a more precise relationship should be derived between the repaired construction and failure modes.

5. Discussion

5.1. Effect of Construct Parameter. Figure 12 shows the relationship between the repaired joint ultimate (P_u) strength and parameters investigated. The grouted clamp significantly enhanced the load-carrying capacity of the joint. For example, the strength of T_3-DR-LCT_{14} was 2.23 times higher than that of T_3-D. Given that the side wall of the grouted clamp can take more load [43], a bare joint with a larger β would yield better reinforcement results. A joint with a smaller γ or d_0 is more susceptible to corrosion [56]. As shown in Figure 12(a), a more severe degree of corrosion leads to a lower repair efficiency for the joint strength.

The primary contribution of a longer sleeve length is the prevention of plastic hinge generation at the sleeve end [34]. If the joint failure is induced by the intersection region, then the extension of the sleeve length will not significantly affect the joint strength (Figure 12(b)). The strength of T_3-DR-$L_{0.7}$

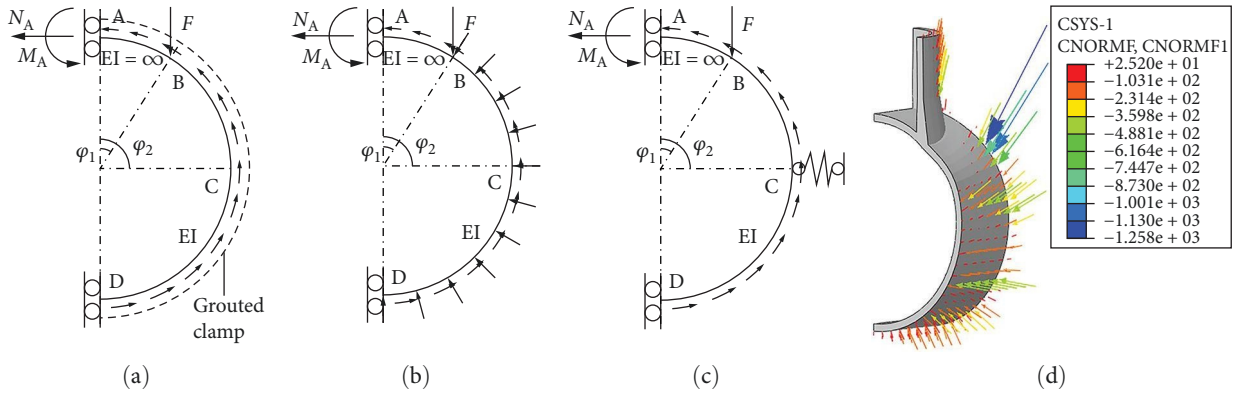

FIGURE 13: Ring models of the repaired joint [59]. (a) 1/2 ring model. (b) 1/2 ring model with simplified confinement. (c) 1/2 ring model with elastic support. (d) Normal direction contact force of T1-DR-L1.

(EDC) was enhanced by only 1.57% as α increased from 0.7 to 1. The sleeve strength imposed a finite effect on P_u (Figure 12(c)), in which the joint strength increased by an average of 7.58% when the sleeve material was changed from Q235 to Q345.

In particular, the effect of the effective thickness of the grouted clamp on the joint strength is related to the failure mode. Instead of facilitating repair, the PHSE caused the grouted clamp to hinder the functioning of the joints. The thicker grout and sleeve did not contribute to the joint strength during brittle failure, as indicated by the proximate flat curves in Figures 12(d) and 12(e). For example, the fluctuation ranges of T_4-DR-ST_6 and T_4-DR-ST_8 were only 1.77%P_u.

In the case of ductile failure of the joint, enhancing the thickness of the grouted clamp had a favorable impact on joint strength [44]. For example, the P_u of T_2-DR-CT_7 closely matched that of T_2-DR-CT_{14}, with both experiencing failure because of PHSE. The extension of the sleeve length in T_2-DR-LCT_{14} yielded a 19.40% increase in P_u when compared to T_2-DR-CT_7, which led to a transition to EDC as the failure mode. Moreover, elevating the grout strength from grade C15 to C30 did not significantly alter the joint strength, as depicted by the nearly flat progression observed in Figure 12(f).

5.2. Ductile Failure Mechanism of Repaired Joint. As a double-skin member, repaired grout compensates for the insufficient chord thickness, and repaired joints have been proven effective based on their load-carrying ability [57] and flexural behavior [58]. The failure modes of the LIC and EDC revealed a joint ductile collapse, which warrants further investigation into the failure mechanism. To the best of the authors' knowledge, a comprehensive theoretical approach for T-joints with grouted clamps has not been developed to date. Zuo [59] proposed an improved theoretical model for a grout-filled GFRP T-joint (Figure 13(a)–13(c)) based on a typical ring model [50].

As shown in Figure 13(a), the confined joint was simplified as a half-section on the sliding support. The saddle point was assumed to be a yield hinge directly affected by a concentrated load. This simplification is consistent with the basic theoretical concept of van der Vegte's [50] study. Under a specific assumption regarding the grouted clamp, the surrounding restriction on the joint surface was resolved into uniform tangential and normal forces (Figure 13(b)). The restriction on the lateral bulge of the chord is replaced by an elastic support ($\phi_2 = 1/2\pi$), as shown in Figure 13(c).

The confinement effect of the grouted clamp on T_1-DR-L_1 (Figure 13(d)) was investigated at its ultimate strength. The contact force of the joint surface element (5 mm × 5 mm) was extracted to reflect the behavior in the normal direction. The grouted clamp did not offer a uniform restraint force, and the chord indentation resulted in a compound distribution. Restraint to the chord bulge was provided by the confinement of the entire interaction surface of the grouted clamp. The failure mechanism of the repaired joint was complex, and the numerical simulation results did not confirm the simplified mechanism proposed by Zuo [59]. Numerical analysis offers a more comprehensive understanding of grouted clamps; however, their actual failure mechanism requires further investigation.

5.3. Predicted Strength Equation. To facilitate the convenient repair of corroded T-joints with grouted clamps, in this study, the proposed strength equation for the repaired joint is discussed. To the best of the authors' knowledge, no existing publication has proposed a strength equation specifically for the reinforcement method involving grouted clamps. In reviewing related research on concrete-filled double skin joints, Hou [60–62] suggested strength prediction models, such as Equations (1)–(3), which consider the confinement effect of the grout and circular cross-section of tubular structures:

$$N_{CFST} = 2f_{ck}\frac{A_1}{\sin\theta}\sqrt{A_2/A_1}, \tag{1}$$

$$A_1 = \frac{\pi d_w^2}{4}, \tag{2}$$

$$A_2 = \frac{A_1}{\sin\theta} + 2b_0 b_1, \tag{3}$$

where NCFST represents the load-bearing capacity of the concrete-filled double skin joint, A_1 denotes the contact

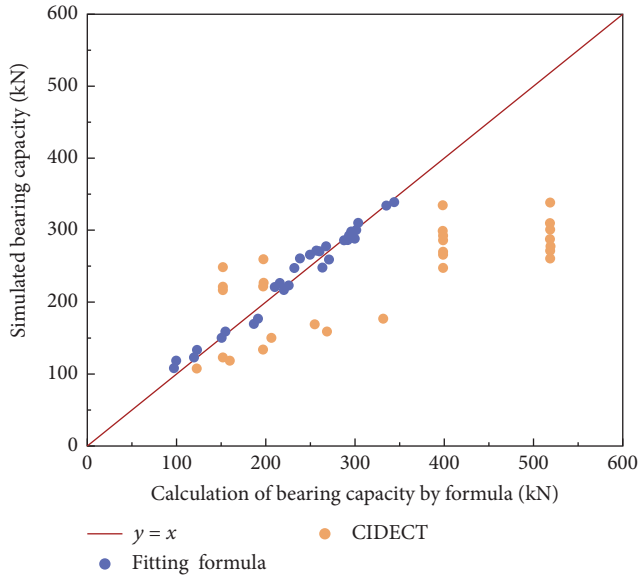

FIGURE 14: Error comparison of the proposed and CIDECT [21] equations.

bearing area, A_2 denotes the dispersed bearing area, f_{ck} denotes the characteristic compressive strength of the concrete, and θ denotes the angle between the chord and brace in the tubular joint.

The aforementioned equations were derived and modified from those proposed by CIDECT [21], which offer a notable extension to the strength calculation equation for an original joint under brace compression, as presented in Equation (4). The equation can be applied conveniently to grouted members by substituting t_0 with the effective chord thickness (t_e), as shown in Equation (5), where f_{y0} refers to the chord coupon yield stress and t_i denotes the reinforcement thickness:

$$P_u = 2.6 \times (1 + 6.8\beta^2) \times \gamma^{0.2} \times f_{y0} \times t_0^2, \tag{4}$$

$$t_e = \sqrt{t_0^2 + t_i^2}. \tag{5}$$

This calculation model is related to the joint failure of chord plastification under brace compression. The repaired joint models that succumbed to failure via LIC or EDC conformed to the specified failure criteria. Despite the discrepancy between the actual corrosion defects and reinforcement from the assumed joint geometry, the abovementioned equations were utilized to estimate the strength of the repaired joints in this study. Figure 14 presents a comparison of the predicted equation's results against those of the numerical models, where the diagonal represents the ultimate strength as determined by the models. The chord thickness within the corroded area was factored into the calculations as t_0. The standard equation yielded results that deviated, often predicting strengths higher than those observed in simulations. This discrepancy arises because Equations (4) and (5) were originally intended for joints with fully grouted chords, which leads to overestimated results for joints with grouted clamps. Consequently, there is a clear need for a predictive equation that accurately reflects the characteristics of grouted clamps.

Considering the more convenient expression of corroded thickness, t_μ was introduced (Equation (6)), wherein μ refers to corrosion degree corresponding to the specimen label. Additionally, the usage of t_μ could imply an intact joint if μ corresponds to zero:

$$t_\mu = (1 - \mu)t_0. \tag{6}$$

Furthermore, the conceptual simplification method of t_e to grouted chord ignores the material strength and structure characteristic of grouted clamp. Hou [60–62] supposed the insufficiency of standard equations for a grouted double-skin joint. Based on the aforementioned analysis results, a modified resistance equation was developed for a joint with grouted clamp, as indicated in Equation (7), which eliminated the inadequate function of t_e:

$$P_u = (1 + k_1\beta^2) \times \gamma^{k_2} \times \left[k_3 \times t_\mu^2 \times f_{y0} + (1 + \alpha)^{k_4} \times (k_5 \times t_s^2 \times f_s + k_6 \times t_c^2 \times f_c)\right], \tag{7}$$

where f_s denotes the sleeve yield strength and f_c denotes the grout compressive strength. k_1–k_6 refer to the regression factor. The installation of the grouted clamp modified the joint's primary nondimensional parameters (β and γ), which were adjusted by the coefficients k_1 and k_2. It is noteworthy that this refined formulaic model also considered the failure criteria associated with chord plastification. The capacity for plastic deformation of the chord, grouted layer, and sleeve was encapsulated in the model in a unified manner. Nevertheless, the constants k_3, k_5, and k_6 should not be construed as weighting coefficients for joint resistance, as they pertain specifically to the sleeve length coefficient's influence.

SPSS [63] was chosen to evaluate the fitness and applicability, resulting in the derivation of a comprehensive practical equation presented in Equation (8). The data used for this analysis excluded joint models that failed in PHSE. The applicability of Equation (8) is limited to joints failing in LIC or EDC, with the validity of structural parameters specified as follows: $0 \le \mu \le 0.3$, $0.4 \le \beta \le 0.8$, $10 \le 2\gamma \le 30$, $\mu \le 30\%$, $a \ge 1$, 4 mm $\le t_s \le$ 6 mm, 235 MPa $\le f_s \le$ 460 MPa, 7 mm $\le t_c \le$ 14 mm, $f_c \ge$ 22 MPa, and 235 MPa $\le f_y \le$ 460 MPa:

$$P_u = (1 + 0.2\beta^2) \times \gamma^{0.473} \times \left[2.986 \times t_\mu^2 \times f_{y0} + (1 + \alpha)^{0.1} \times (2.12 \times t_s^2 \times f_s + 3.788 \times t_c^2 \times f_c)\right]. \tag{8}$$

The fitting and simulation results presented as scatter diagrams in Figure 14 indicate a good agreement. The ratios of the calculated results to the modeling results, variance, and R^2 were 0.995, 0.003, and 0.973, respectively. The calculation error was confined to (−10%, 15%), which confirms that the results yielded by the modified equation are suitable for the current study.

6. Conclusions

In this study, FE analysis was employed to investigate the reinforcement effectiveness of grouted clamps on uniformly corroded T-joints. The fidelity of the FE simulations was confirmed by comparison with actual experimental results. A total of 56 numerical models were developed, incorporating variations in joint geometry, corrosion depth, and the construction of the grouted clamp. The study analyzed the failure modes and assessed the ultimate strength of the repaired joints. Stress distribution patterns were scrutinized to understand the reinforcement mechanism provided by the grouted clamp. Drawing on the CIDECT [9] standards for tubular joints, a revised strength prediction equation was introduced. The key findings of this research are summarized as follows:

(i) The failure of the repaired specimens was initiated by a gradual progression of plasticity in the intersection region, resulting in acceptable ductile failure modes. A moderate corrosion depth, not exceeding $30\%d_0$, did not alter the failure mode of the repaired joint. However, improper fabrication of the grouted clamp could lead to the formation of a plastic hinge at the end of the sleeve, causing the joint to fail in a brittle manner and the load–displacement curve to end abruptly.

(ii) For preventing the brittle failure of repaired T-joint using grouted clamp, the weight and thickness of reinforcement should be limited, and the overlapping ratio of the sleeve on the chord should exceed 0.7.

(iii) The grouted clamp effectively enhanced the static performance of the corroded joint, with the ultimate strength of the repaired joint reaching up to 2.23 times that of the corroded joint. In the case of ductile failure of the repaired joint, increasing the thickness of the grouted sleeve substantially increased the joint's strength.

(iv) The existing ring model of the outer grouted reinforcement could conceptually explain the similar confinement action of the grouted clamp to the corroded joint. However, the numerical results demonstrated more complex restraint conditions of the grouted clamp.

(v) A new modified equation for repaired joint strength was proposed for engineering application, and a good agreement was observed between the calculated and test results within the scope of the parameters.

Nomenclature

b_1: Chord outer diameter
t_1: Chord wall thickness
L_1: Chord length
b_0: Brace outer diameter
t_0: Brace wall thickness
L_0: Brace length
β: Brace width-to-chord width ratio (b_1/b_0)
γ: Chord width-to-twice chord thickness ($b_0/2t_0$)
E: Yong's modulus of steel material
f_y: Yield stress of steel material
f_u: Ultimate stress of steel material
C: Strength degree of grout
Q: Strength degree of sleeve
f_s: Yield stress of sleeve
t_c: Grout thickness
t_s: Sleeve thickness
α: Ratio of the sleeve overlapping length to the diameter of the corresponding components length
f_{y0}: Yield stress of chord
t_i: Reinforcement thickness
μ: Corrosion degree to chord thickness
t_μ: Function of corroded thickness.

Data Availability

Data generated or analyzed during this study are provided in full within the published article.

Conflicts of Interest

The authors declare that they have no conflicts of interest.

Acknowledgments

The authors would like to thank Editage (https://www.editage.cn) for English language editing.

References

[1] Z. Yu and J. Amdahl, "A review of structural responses and design of offshore tubular structures subjected to ship impacts," *Ocean Engineering*, vol. 154, pp. 177–203, 2018.

[2] W. Dong, T. Moan, and Z. Gao, "Fatigue reliability analysis of the jacket support structure for offshore wind turbine considering the effect of corrosion and inspection," *Reliability Engineering & System Safety*, vol. 106, pp. 11–27, 2012.

[3] Det Norske Veritas, "Design of offshore wind turbine structures (DNV-OS-J101)," Copenhagen, Denmark, 2014.

[4] International Organization for Standardization, *Petroleum and Natural Gas Industries—Fixed Steel Offshore Structures*, ISO, 2007.

[5] T. K. Fataliyev and S. A. Mehdiyev, "Analysis and new approaches to the solution of problems of operation of oil and gas complex as cyber-physical system," *International Journal of Information Technology and Computer Science*, vol. 10, no. 11, pp. 67–76, 2018.

[6] H. Nassiraei, "Local joint flexibility of CHS T/Y-connections strengthened with collar plate under in-plane bending load: parametric study of geometrical effects and design formulation," *Ocean Engineering*, vol. 202, Article ID 107054, 2020.

[7] H. Nassiraei, "Probability distribution models for the ultimate strength of tubular T/Y-joints reinforced with collar plates at room and different fire conditions," *Ocean Engineering*, vol. 270, Article ID 113557, 2023.

[8] H. Nassiraei, "Static strength of tubular T/Y-joints reinforced with collar plates at fire induced elevated temperature," *Marine Structures*, vol. 67, Article ID 102635, 2019.

[9] H. Nassiraei, M. A. Lotfollahi-Yaghin, and H. Ahmadi, "Structural behavior of tubular T/Y-joints with collar plate under static in-plane bending," *Journal of Constructional Steel Research*, vol. 123, pp. 121–134, 2016.

[10] H. Nassiraei, M. A. Lotfollahi-Yaghin, and H. Ahmadi, "Static performance of doubler plate reinforced tubular T/Y-joints subjected to brace tension," *Thin-Walled Structures*, vol. 108, pp. 138–152, 2016.

[11] H. Nassiraei, M. A. Lotfollahi-Yaghin, and H. Ahmadi, "Static strength of doubler plate reinforced tubular T/Y-joints subjected to brace compressive loading: study of geometrical effects and parametric formulation," *Thin-Walled Structures*, vol. 107, pp. 231–247, 2016.

[12] H. Nassiraei and P. Rezadoost, "Stress concentration factors in tubular T-joints reinforced with external ring under in-plane bending moment," *Ocean Engineering*, vol. 266, Article ID 112551, 2022.

[13] M. F. Muda, M. H. M. Hashim, M. K. Kamarudin et al., "Burst pressure strength of corroded subsea pipelines repaired with composite fiber-reinforced polymer patches," *Engineering Failure Analysis*, vol. 136, Article ID 106204, 2022.

[14] T. Tafsirojjaman, S. Fawzia, D. P. Thambiratnam, and X.-L. Zhao, "FRP strengthened SHS beam-column connection under monotonic and large-deformation cyclic loading," *Thin-Walled Structures*, vol. 161, Article ID 107518, 2021.

[15] T. Tafsirojjaman, S. Fawzia, D. P. Thambiratnam, and X. L. Zhao, "Behaviour of CFRP strengthened SHS beams subjected to impact load: experimental and FE study," *Engineering Structures*, vol. 229, Article ID 111681, 2021.

[16] T. Tafsirojjaman, D. P. Thambiratnam, N. H. R. Sulong, and S. Fawzia, "Performance of CFRP strengthened full-scale SHS connections subjected to cyclic loading," *Thin-Walled Structures*, vol. 175, Article ID 109211, 2022.

[17] H. Nassiraei and P. Rezadoost, "Static capacity of tubular X-joints reinforced with fiber reinforced polymer subjected to compressive load," *Engineering Structures*, vol. 236, Article ID 112041, 2021.

[18] H. Nassiraei and P. Rezadoost, "Stress concentration factors in tubular T/Y-joints strengthened with FRP subjected to compressive load in offshore structures," *International Journal of Fatigue*, vol. 140, Article ID 105719, 2020.

[19] T. Tafsirojjaman, S. Fawzia, and D. P. Thambiratnam, "Structural behaviour of CFRP strengthened beam-column connections under monotonic and cyclic loading," *Structures*, vol. 33, pp. 2689–2699, 2021.

[20] China Planning Press, "Steel structure design standard (GB-50017)," Beijing, PRC, 2017.

[21] CIDECT, *Design Guide for Circular Hollow Section (CHS) Joints under Predominantly Static Loading*, Committee for International Development and Education on Construction of Tubular Structures,GER, 2008.

[22] European Committee for Standardization, "Eurocode 3-design of steel structures (EC3)," UK, 2011.

[23] M. R. U. Kawsar, S. A. Youssef, M. Faisal, A. Kumar, J. K. Seo, and J. K. Paik, "Assessment of dropped object risk on corroded subsea pipeline," *Ocean Engineering*, vol. 106, pp. 329–340, 2015.

[24] R. Wang and R. A. Shenoi, "Experimental and numerical study on ultimate strength of steel tubular members with pitting corrosion damage," *Marine Structures*, vol. 64, pp. 124–137, 2019.

[25] S. Xu, H. Wang, A. Li, Y. Wang, and L. Su, "Effects of corrosion on surface characterization and mechanical properties of butt-welded joints," *Journal of Constructional Steel Research*, vol. 126, pp. 50–62, 2016.

[26] C. G. Soares and Y. Garbatov, "Reliability of maintained ship hull girders subjected to corrosion and fatigue," *Structural Safety*, vol. 20, no. 3, pp. 201–219, 1998.

[27] A. C. Benjamin and E. Andrade, "Modified method for the assessment of the remaining strength of corroded pipelines," in *Rio Pipeline 2003 Conference and Exposition*, pp. 1–14, Instituto Brasileiro de Petróleo e Gás - IBP, Rio de Janeiro, RJ, 2003.

[28] L. D. Lutes, T. L. Kohutek, B. K. Ellison, and K. F. Konen, "Assessing the compressive strength of corroded tubular members," *Applied Ocean Research*, vol. 23, no. 5, pp. 263–268, 2001.

[29] Y.-B. Shao, Z.-M. Chen, and Z.-L. Zhou, "Experimental on static bearing capacity of corroded T-joints strengthened with CFRP," *Journal of Civil Engineering and Management*, vol. 37, no. 5, pp. 15–19, 2020.

[30] W. Zuo, H. Chang, Z. Li, A. An, J. Xia, and T. Yu, "Experimental investigation on compressive behavior of corroded thin-walled CHS T-joints with grout-filled GFRP tube repairing," *Thin-Walled Structures*, vol. 175, Article ID 109222, 2022.

[31] S. Rodrigues, C. Restrepo, E. Kontos, R. T. Pinto, and P. Bauer, "Trends of offshore wind projects," *Renewable and Sustainable Energy Reviews*, vol. 49, pp. 1114–1135, 2015.

[32] X. L. Kang, H. T. Zhao, J. Y. Xue, and J. B. Wu, "Theoretic analysis for hooping mechanism and composite elastic modulus of cfst members," *Engineering Mechanics*, vol. 24, no. 11, pp. 121–125, 2007.

[33] N. V. Chellappan and S. Nallayarasu, "Experimental and numerical investigation on axial load transfer across cracked tubular joint strengthened with grouted clamps of a jacket in under water condition," *Ships and Offshore Structures*, vol. 17, no. 8, pp. 1717–1730, 2022.

[34] S. Jiang, X. Guo, Z. Xiong, Y. Cai, and S. Zhu, "Experimental studies on behaviour of tubular T-joints reinforced with grouted sleeve," *Steel and Composite Structures*, vol. 23, no. 5, pp. 585–596, 2017.

[35] C. Chilvers, *Analysis of the structural behaviour of grouted pile/sleeve connections for offshore structures*, Ph.D. dissertation, City University London, London, UK, 1984.

[36] M. Smith, *Abaqus 2016 Documentation*, Dassault Systemes Company, Paris, FR, 2016.

[37] J. A. Packer, *A theoretical analysis of welded steel joints in rectangular hollow sections*, Ph.D. dissertation, University of Nottingham, Nottingham, UK, 1978.

[38] P. Deng, X. Chen, B. Yang, J. Guo, and Y. Liu, "Finite element analysis on the residual bearing capacity of axially preloaded tubular T-joints subjected to impacts," *Structures*, vol. 31, pp. 286–304, 2021.

[39] W. Li, L.-H. Han, and T.-M. Chan, "Numerical investigation on the performance of concrete-filled double-skin steel tubular members under tension," *Thin-Walled Structures*, vol. 79, pp. 108–118, 2014.

[40] D. Jin, C. Hou, and L. Shen, "Effect of welding residual stress on the performance of CFST tubular joints," *Journal of Constructional Steel Research*, vol. 184, Article ID 106827, 2021.

[41] H.-T. Li and B. Young, "Behaviour of concrete-filled ferritic stainless steel tubular joints: experimental investigation, numerical modelling and design," *Engineering Structures*, vol. 247, Article ID 113109, 2021.

[42] M. Pandey, K.-F. Chung, and B. Young, "Design of cold-formed high strength steel tubular T-joints under compression loads," *Thin-Walled Structures*, vol. 164, Article ID 107573, 2021.

[43] L. H. Lu, G. D. D. Winkel, Y. Yu, and J. Wardenier, "Deformation limit for the ultimate strength of hollow section joints," in *Tubular Structures VI*, pp. 341–347, Routledge, 2021.

[44] R. Harwood and E. Shuttleworth, *Grouted and Mechanical Strengthening and Repair of Tubular Steel Offshore Structures*, HM Stationery Office, London, UK, 1988.

[45] C. J. Zhang, H. H. Zhang, X. Shi, J. R. Chen, and L. Zhou, "Design method of an expansive stressed grouted clamp on a joint of a jacket platform," in *Proceedings of the 26th International Ocean and Polar Engineering Conference*, One Petro, Rhodes, GR, 2016.

[46] China Architecture & Building Press, "Code for design of concrete structures (GB-50010)," Beijing, PRC [In Chinese], 2002.

[47] P. Costa and R. B. Gidro, "Behavior assessment of asymmetrical building with concrete damage plasticity (CDP) under seismic load," in *Proceedings of the XLI Ibero-Latin-American Congress on Computational Methods in Engineering*, Brazilian Association of Computational Methods in Engineering (ABMEC), 2020.

[48] Q.-Y. Wang, S.-L. Bai, and Z.-D. Liu, "Surface characterization and erosion–corrosion behavior of Q235 steel in dynamic flow," *Tribology Letters*, vol. 53, no. 1, pp. 271–279, 2014.

[49] Q. Hui, H. Jingsi, and Q. Chao, "Experimental study on tubular T-joints under drop hammer impact loads," *Journal of Building Structures*, vol. 34, no. 4, pp. 65–73, 2013.

[50] G. J. van der Vegte, *The Static Strength of Uniplanar and Multiplanar Tubular T- and X- joints*, Delft University Press, 1995.

[51] A. P. Voth and J. A. Packer, "Numerical study and design of T-type branch plate-to-circular hollow section connections," *Engineering Structures*, vol. 41, no. 1, pp. 477–489, 2012.

[52] X.-L. Zhao, J. Wardenier, J. A. Packer, and G. J. van der Vegte, "Current static design guidance for hollow-section joints," *Proceedings of the Institution of Civil Engineers-Structures and Buildings*, vol. 163, no. 6, pp. 361–373, 2010.

[53] X. Ma, W. Wang, Y. Chen, and X. Qian, "Simulation of ductile fracture in welded tubular connections using a simplified damage plasticity model considering the effect of stress triaxiality and Lode angle," *Journal of Constructional Steel Research*, vol. 114, pp. 217–236, 2015.

[54] R. Feng and B. Young, "Theoretical analysis of cold-formed stainless steel tubular joints," *Engineering Structures*, vol. 83, pp. 99–115, 2015.

[55] Y. S. Choo, G. J. van der Vegte, N. Zettlemoyer, B. H. Li, and J. Y. R. Liew, "Static strength of T-Joints reinforced with doubler or collar plates. I: experimental investigations," *Journal of Structural Engineering*, vol. 131, no. 1, pp. 119–128, 2005.

[56] Y. Bai, Y. Kim, H.-B. Yan, X.-F. Song, and H. Jiang, "Reassessment of the jacket structure due to uniform corrosion damage," *Ships and Offshore Structures*, vol. 11, no. 1, pp. 105–112, 2016.

[57] J. W. Park and S. M. Choi, "Structural behavior of CFRP strengthened concrete-filled steel tubes columns under axial compression loads," *Steel and Composite Structures*, vol. 14, no. 5, pp. 453–472, 2013.

[58] Y. Idris and T. Ozbakkaloglu, "Flexural behavior of FRP-HSC-steel composite beams," *Thin-Walled Structures*, vol. 80, pp. 207–216, 2014.

[59] W. Zuo, *Compressive bearing mechanism and design methods of grout-filled GFRP repairing corroded tubular joint*, M.D. dissertation, China University of Mining and Technology, Xuzhou, PRC, 2020.

[60] C. Hou, L.-H. Han, and X.-L. Zhao, "Behaviour of circular concrete filled double skin tubes subjected to local bearing force," *Thin-Walled Structures*, vol. 93, pp. 36–53, 2015.

[61] C. Hou, L.-H. Han, and X.-L. Zhao, "Concrete-filled circular steel tubes subjected to local bearing force: experiments," *Journal of Constructional Steel Research*, vol. 83, no. 1, pp. 90–104, 2013.

[62] C. Hou, L.-H. Han, and X.-L. Zhao, "Concrete-filled circular steel tubes subjected to local bearing force: finite element analysis," *Thin-Walled Structures*, vol. 77, no. 1, pp. 109–119, 2014.

[63] J. Pallant, *SPSS Survival Manual*, Routledge, 2020.